Crumpling of silver nanowires by endolysosomes strongly reduces toxicity

Sylvia G. Lehmann[a], Djadidi Toybou[a,b], Ana-Elena Pradas del Real[c], Devrah Arndt[d], Abderrahmane Tagmount[d], Muriel Viau[a], Malak Safi[a], Alexandra Pacureanu[c], Peter Cloetens[c], Sylvain Bohic[c,e], Murielle Salomé[c], Hiram Castillo-Michel[c], Brenda Omaña-Sanz[f,g,h], Annette Hofmann[f,g,h], Christopher Vulpe[d], Jean-Pierre Simonato[b], Caroline Celle[b], Laurent Charlet[a], and Benjamin Gilbert[a,i,1]

[a]Institut des Sciences de la Terre, Université de Grenoble–Alpes, CNRS, F-38000 Grenoble Cedex 9, France; [b]Laboratoire d'Innovation pour les Technologies des Energies Nouvelles et les Nanomatériaux, Département des Technologies des Nouveaux Matériaux, Université de Grenoble–Alpes, Commissariat à l'Énergie Atomique et aux Énergies Alternatives, F-38054 Grenoble Cedex 9, France; [c]European Synchrotron Radiation Facility, Course Spéciale (CS) 40220, 38043 Grenoble Cedex 9, France; [d]Center for Environmental and Human Toxicology, Department of Physiological Sciences, College of Veterinary Medicine, University of Florida, Gainesville, FL 32611; [e]Synchrotron Radiation for Biomedicine, CS 40220, Institut National de la Santé et de la Recherche Médicale, 38043 Grenoble Cedex 9, France; [f]Laboratoire d'Océanologie et de Géosciences (LOG), UMR 8187, Université Lille, F 59000 Lille, France; [g]UMR 8187, CNRS, F 59000 Lille, France; [h]UMR 8187, Université Littoral Côte d'Opale, F 62930 Wimereux, France; and [i]Energy Geoscience Division, Lawrence Berkeley National Laboratory, Berkeley, CA 94720

Edited by Howard A. Stone, Princeton University, Princeton, NJ, and approved June 12, 2019 (received for review November 23, 2018)

Fibrous particles interact with cells and organisms in complex ways that can lead to cellular dysfunction, cell death, inflammation, and disease. The development of conductive transparent networks (CTNs) composed of metallic silver nanowires (AgNWs) for flexible touchscreen displays raises new possibilities for the intimate contact between novel fibers and human skin. Here, we report that a material property, nanowire-bending stiffness that is a function of diameter, controls the cytotoxicity of AgNWs to nonimmune cells from humans, mice, and fish without deterioration of critical CTN performance parameters: electrical conductivity and optical transparency. Both 30- and 90-nm-diameter AgNWs are readily internalized by cells, but thinner NWs are mechanically crumpled by the forces imposed during or after endocytosis, while thicker nanowires puncture the enclosing membrane and release silver ions and lysosomal contents to the cytoplasm, thereby initiating oxidative stress. This finding extends the fiber pathology paradigm and will enable the manufacture of safer products incorporating AgNWs.

nanotechnology | endocytosis | fiber toxicity

In the 20th century, the widespread use of high-aspect-ratio asbestos fibers led to adverse health consequences, including pleural mesothelioma, among exposed individuals. Painstaking epidemiology studies led to the establishment of the fiber pathology paradigm (FPP) that defines the distinctive injurious properties of high-aspect-ratio inorganic particles (1). Critical characteristics include biological persistence, mobility, redox reactivity, and proinflammatory capabilities. The replacement of asbestos by vitreous silica fibers eventually led to a decline in asbestos-related diseases in the developed world (2), but the asbestos experience holds considerable relevance for the manufacture and distribution of novel fibrous materials such as metallic nanowires (3).

Silver nanowires (AgNWs) are of considerable utility for consumer electronics because they provide economically and technically competitive approaches for fabricating flexible, optically transparent, and electrically conductive films (4, 5). AgNWs can be deposited from solution onto substrates to form conductive transparent networks (CTNs) that do not degrade by repeated bending. Flexible AgNW-based devices will likely replace existing technology based on doped tin oxide layers on brittle glass sheets for displays and touch screens (6). All AgNW applications balance a range of competing performance and cost characteristics (4) that typically do not include consideration of potential physiological interactions and toxicity.

Because of their morphology and redox reactivity, we (7–9) and other groups (10–13) suspected that AgNWs may exhibit fiber-like toxicity. Indeed, AgNWs exhibit a length threshold for phagocytosis in macrophages (14), induce toxicity in alveolar epithelial cells (15) and provoke numerous indicators of pulmonary toxicity in mice and rats (8, 11). Prior studies, however, have been relevant to pulmonary (i.e., inhalation) exposures, while the anticipated consumer products for AgNWs, including portable electronic devices, suggest the need to evaluate dermal exposure and toxicity. The few studies of nonphagotic cells observed ready internalization of AgNWs through an unidentified endocytosis pathway (9, 15, 16). Although the dermis of healthy human skin provides a barrier to short-term NW exposure (9), we have also observed that AgNWs can translocate through epithelial barriers (7).

The goal of this research collaboration was to establish whether AgNWs could be designed to minimize their intrinsic cellular toxicity while retaining necessary technical properties for CTNs. The link between fiber length and cytotoxicity is well established. The FPP identifies a threshold around 10 μm, above which macrophages cannot successfully internalize nanowires (1) or other nanofibers (17)—this phenomenon called frustrated phagocytosis leads to apoptosis and inflammation. We reasoned that AgNW diameter could be an important control on the extent of internalization via endocytosis. At least 3 endocytotic pathways have been identified that initiate the engulfment of an

Significance

Silver nanowires are a type of novel fiber that are likely to have wide application in consumer electronics but that can also carry risk for cell internalization and toxicity. Here, we show that silver nanowire toxicity can be greatly diminished by reducing nanowire diameter without affecting device performance. X-ray microscopy and supporting studies revealed that endolysosome membranes can mechanically crumple thin silver nanowires, the likely mechanism for diminishing toxicity.

Author contributions: S.G.L., D.A., A.H., C.V., J.-P.S., C.C., L.C., and B.G. designed research; S.G.L., D.T., A.-E.P.d.R., D.A., A.T., M.V., M. Safi, A.P., P.C., S.B., M. Salome, H.C.-M., B.O.-S., and B.G. performed research; D.T., A.T., and P.C. contributed new reagents/analytic tools; S.G.L., A.-E.P.d.R., D.A., A.T., M.V., A.P., P.C., B.O.-S., A.H., C.V., L.C., and B.G. analyzed data; and S.G.L., C.V., J.-P.S., C.C., L.C., and B.G. wrote the paper.

The authors declare no conflict of interest.

This article is a PNAS Direct Submission.

[1]To whom correspondence may be addressed. Email: bgilbert@lbl.gov.

This article contains supporting information online at www.pnas.org/lookup/suppl/doi:10.1073/pnas.1820041116/-/DCSupplemental.

Published online July 8, 2019.

external object by the outer membrane (18) and a common driving force is the free energy of interaction between the object and the outer membrane. Imaging (9) and simulation (19) studies indicate that the internalization of rod-shaped particles occurs via tip–membrane interaction and entry. Smaller diameter objects lower the interaction free energy and raise the energy penalty for membrane curvature. As a consequence, the endocytosis efficiency of nanoparticles and nanorods drops significantly below diameters of 50 to 60 nm, a size at which virus capsids can initiate cell entry without specific molecular interactions that recruit membrane proteins (20). Thus, we sought to establish the effect of AgNW diameter on internalization and toxicity.

Commercial products cover the range of AgNW dimensions required for this study (e.g., refs. 21 and 22) but AgNWs are not commercially available with independent control of length and diameter that in standard syntheses are highly correlated (23). Hence, we performed a multiparameter study of the polyol synthesis method (24, 25) to identify nucleation, growth and purification procedures and conditions to independently vary AgNW diameter and length. We synthesized polyvinylpyrrolidone (PVP)-coated AgNWs with very similar length distributions, around 9 μm and 25 μm, but with mean diameters ranging from 30 to 90 nm (*SI Appendix*, Table S1 and Fig. 1*A*). We assayed the acute cytotoxicity of the AgNWs in three cell lines: murine fibroblasts (Fig. 1*C*), rainbow trout gut cells (Fig. 1*D*) and human primary fibroblasts (*SI Appendix*, Fig. S4) finding in all cases a dose-dependent reduction in cell viability. Following the consensus for nanomaterial dose reporting, we report AgNW dose as number of particles per volume that was calculated from total silver concentration and verified by direct counting. The trends are preserved for doses reported in silver mass concentration (*SI Appendix*, Fig. S2). For ionic silver, a positive control (*SI Appendix*, Fig. S2), the concentration for a 50% reduction in viability (LC_{50}) is in good agreement with prior studies (26).

In accordance with our project hypothesis, we found that AgNW toxicity could be lowered by reducing the diameter of ∼10-μm-long AgNWs. For murine fibroblasts, LC_{50} is almost 2 orders of magnitude higher for 30-nm than for 90-nm-diameter nanowires (Fig. 1*C*). For rainbow trout gut cells the dose–response curves show ∼1 order of magnitude reduction in toxicity (Fig. 1*D*). In accordance with the FPP, 25-μm-long AgNWs are significantly more cytotoxic than ∼10-μm-long NWs, confirming that a "frustrated endocytosis" mechanism applies to fiber exposure in nonphagocytic cells. Counter to our hypothesis, however, reducing the diameter of ∼25-μm-long AgNWs had only a small reduction in toxicity, suggesting diameter did not primarily affect internalization. We used dark-field visible light microscopy to compare the uptake of 30- versus 90-nm-diameter, ∼10-μm-long AgNWs by murine fibroblasts (*SI Appendix*, Fig. S3). In each case, close to 100% of the administered AgNWs were internalized within 24 h. We further checked for differences in the release of ionic silver in the cell culture media finding it to be around 0.4 μg/mL for the smallest and 0.3 μg/mL for the largest-diameter AgNWs (*SI Appendix*, Fig. S1), values that are significantly below the 50% lethal dose (LD_{50}) for silver nitrate and run counter to the toxicity trends. Based on all these findings, the differential toxicity must be caused by physiological interactions following internalization.

We used a combination of synchrotron X-ray imaging and microchemical analysis methods at beamlines ID-16A and ID-21 at the European Synchrotron Radiation Facility (ESRF) to study the intracellular location, morphology and chemistry of 33- or 93-nm diameter, 9-μm long, AgNWs administered to murine fibroblasts cultured on X-ray transparent Si_3N_4 membranes, cryofixed immediately before analysis and analyzed at 120 K to minimize X-ray radiation damage. Holographic X-ray nanoimaging generated 2D projection images (phase contrast maps) and stereographic images with ∼40-nm resolution. Full 3D reconstructions with ∼80-nm resolution were obtained from holotomography. Nanofocus X-ray fluorescence (XRF) of the same specimens provided 2D elemental maps with ∼40-nm resolution. Microfocus XRF of duplicate samples provided 2D elemental maps that could be complemented by Ag L_{III}-edge X-ray absorption spectra to determine silver speciation. Key findings from these data are summarized in Fig. 2.

The X-ray images revealed a striking difference in the intracellular fate of AgNWs with different diameters. Intracellular 93-nm AgNWs were slightly bent with respect to nanowires after synthesis and suspension in cell culture media but nevertheless retained the elongate nanowire morphology (Fig. 2*A*).

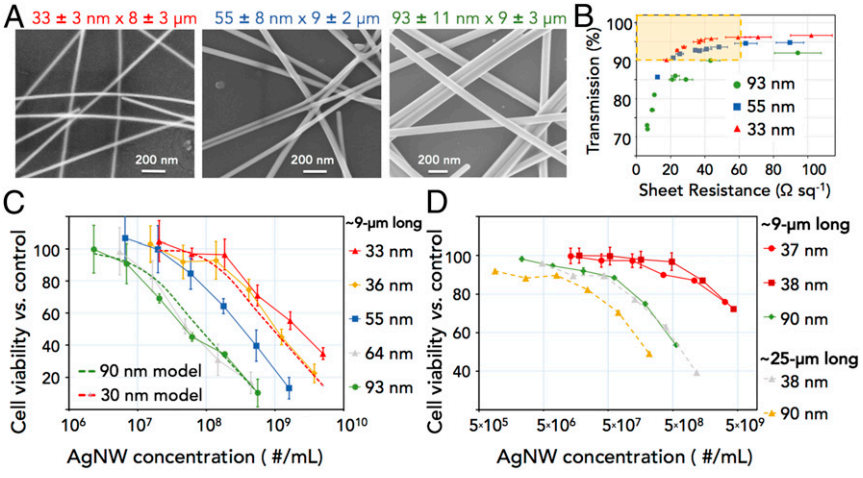

Fig. 1. Diameter-dependent performance and cytotoxicity of AgNWs. (*A*) Scanning-electron microscopy images of 8- to 9-μm long AgNW with 3 mean diameters. (*B*) Relationship between optical transparency and sheet resistance for CTNs fabricated by ∼9-μm-long AgNWs with three different diameters. Each data point represents a spray-coated network at a different AgNW density. Yellow-shaded region represents the technological target for commercial CTNs. (*C*) Viability of murine fibroblasts cells following 24-h exposure with AgNWs of different diameter, as determined by the MTT assay. The dashed lines are model predictions as described in the text. (*D*) Viability of rainbow trout gut cells following 24-h exposure with AgNWs of different diameter determined by CellTiter-Glo assay. Cell-viability data are presented as a percentages relative to the nontreated control cells. Error bars on triplicate measurements are 1 SD.

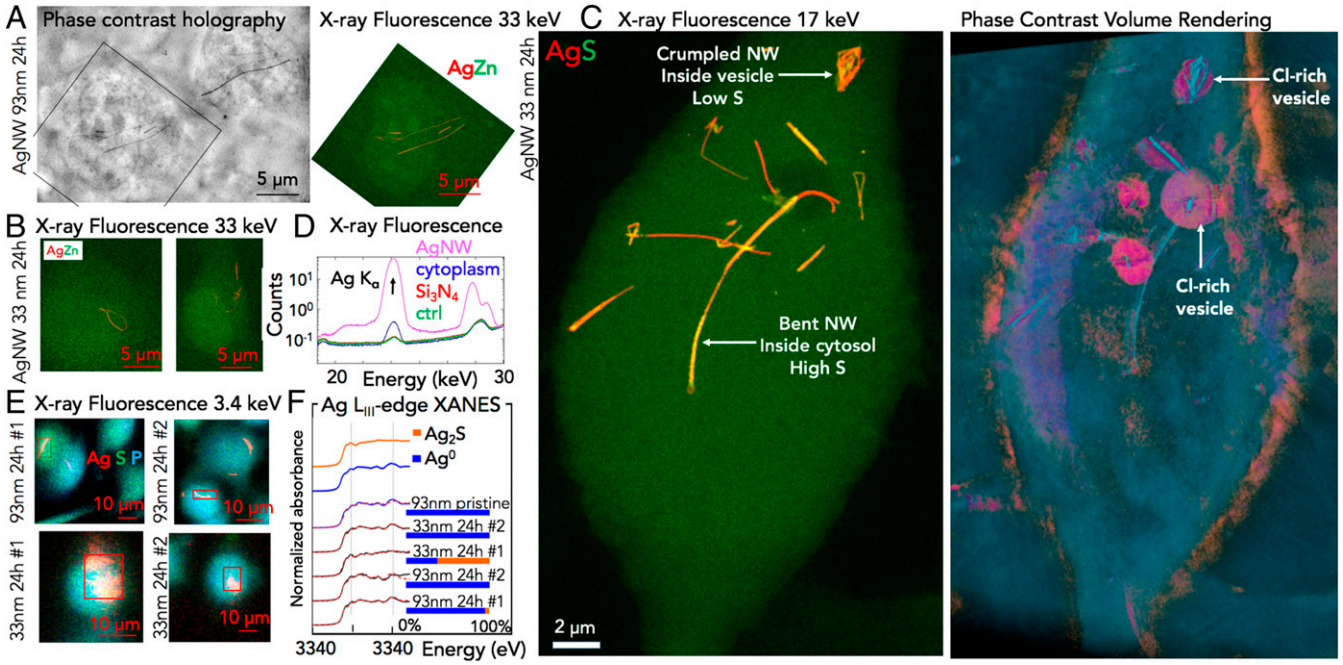

Fig. 2. X-ray analyses of murine fibroblasts exposed to 33- or 93-nm diameter and ∼9-μm-long AgNWs. (*A*) Phase-contrast image (*Left*) and nanofocus Zn and Ag elemental map (*Right*) of two cells containing 93-nm AgNW acquired at 33 keV. (*B*) Elemental maps acquired at 33 keV of cells exposed to 33-nm AgNW. (*C*) Elemental map (*Left*) and phase-contrast image (*Right*) acquired at 17 keV of a fibroblast cell exposed to 33-nm AgNW. Yellow regions of the left image indicate colocalization of Ag and S. An animated 3D tomogram is given in Movie S1. (*D*) X-ray fluorescence spectra from internalized AgNWs and cytoplasm of exposed cell, control cell ("ctrl") and X-ray transparent substrate (Si_3N_4). (*E*) Examples of microfocus elemental maps of cells exposed to 33- and 93-nm-diameter AgNW. (*F*) Selected area Ag L_{III}-edge XANES spectra from reference materials and AgNWs incubated in cell culture medium ("pristine") or exposed to cells for 24 h. Names of the spectra correspond to images given in *E*. Dashed lines are linear combination fits of reference spectra to the data and the bars represent the proportion of Ag_2S and Ag^0 determined by the fitting.

By contrast, the majority of intracellular 33-nm AgNWs were completely deformed and exhibited crumpled, collapsed, and even circular shapes (Fig. 2*B*).

A combined XRF and tomographic analysis at 17 keV of a single fibroblast cell exposed to 30-nm-diameter AgNWs for 24 h provided more insight into the internalization pathway and AgNW fate (Fig. 2*C* and Movie S1). All AgNWs were associated with chlorine-rich intracellular vesicles we infer to be late endosomes or lysosomes (18). One crumpled AgNW is completely contained within a vesicle and has a low association of sulfur with silver. One bent but elongate AgNW has only the tip clearly contained. That tip has low sulfur, but in contrast region that extends away from the vesicle is extensively associated with sulfur. Ag L_{III}-edge X-ray absorption near-edge structure (XANES) showed that 33- and 93-nm-diameter AgNWs that were internalized underwent varying degrees of sulfidation to form Ag_2S, a reaction that did not occur over 7 d in cell-free culture medium (Fig. 2*F*). Silver organosulfur species and silver chloride were not detectable. Integrating the Ag K_α fluorescence from selected areas provided evidence of an above-background signal from diffuse silver inside the cytoplasm of a cell containing 93-nm AgNWs but not neighboring cells without AgNWs or cells exposed to 33-nm AgNWs.

Cellular injury caused by nanomaterial exposure typically falls within an oxidative-stress hierarchy in which the generation of reactive oxygen species (ROS) affects cellular physiology, causes proinflammatory responses and ultimately cell death (27, 28). Murine fibroblast cells were exposed to 10^6 to 10^8 NW/mL of 36- or 93-nm-diameter AgNWs for 24 h, and we used fluorescent probes and epifluorescence microscopy to assess selected cellular responses. Using a fluorescent probe for general ROS (CM-H2DCFDA), we determined dose–response for the 2 AgNW diameters, finding no intracellular ROS production at the lowest dose but an increasing dose–response for the 93-nm AgNWs (Fig. 3 *A* and *D*). Using a probe for mitochondrial membrane potential, ψ_m, (JC-1) we find, at equivalent doses, that 93-nm but not 36-nm-diameter AgNWs cause substantial reduction of ψ_m (Fig. 3 *B* and *D*). Intracellular calcium release from storage sites such as the endoplasmic reticulum is a major oxidative stress response associated with mitochondrial perturbation and cell death. Using a probe for Ca^{2+} (Fluo-4 AM) we find, at equivalent doses, that 93-nm but not 36-nm AgNWs provoke substantial calcium release (Fig. 3 *C* and *D*). Apoptotic cells loose membrane integrity which can be assessed by the uptake of propidium iodide (PI). Only cultures exposed to 93-nm AgNWs showed PI permeant cells (Fig. 3 *C* and *D*). Thus, the fluorescence assays demonstrate that 93-nm AgNWs provoke a significantly stronger cytotoxic response.

These findings demonstrate that the cytotoxicity of AgNWs shorter than ∼10 μm is determined by the ability to puncture the enclosing endocytotic membranes during internalization and processing. Endolysosome puncturing could initiate an oxidative stress response by 2 pathways. First, we find that exposure to the cytoplasm initiates or accelerates oxidative sulfidation of silver. Although precipitation as a sulfide strongly reduces the activity of ionic silver (15), sulfidation is a complex redox reaction that can generate radicals (29) and deplete H_2S, a signaling molecule with antioxidant properties (30). Second, membrane puncturing could release lysosomal contents including acids and proteases that can initiate stress responses (31). Indeed, AgNWs are more effective than Ag nanoparticles at the induction of NLRP3 inflammasome activation and IL-1β production in phagocytes but until now a mechanism for membrane damage has not been clearly revealed (32, 33).

Further evidence that AgNWs can puncture lipid bilayer membranes is provided by studies of AgNW phagocytosis by rat

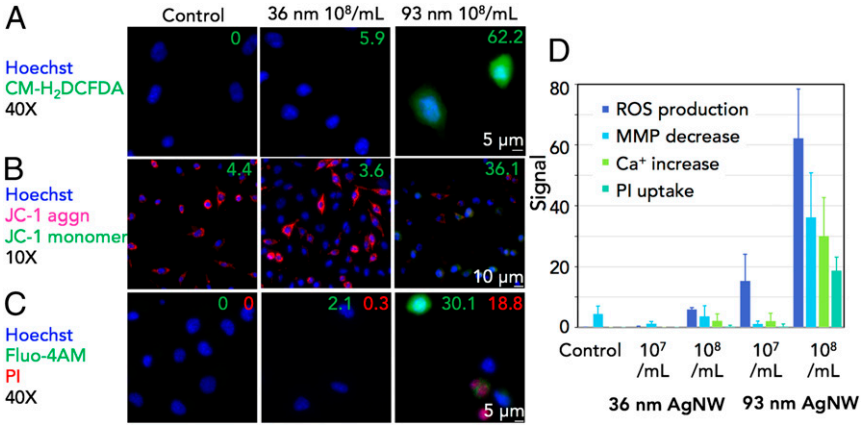

Fig. 3. Fluorescence assays of diameter dependent cellular toxicity. (*A–C*) Merged epifluorescence images of murine fibroblast cells exposed to 10^8 NW/mL of 36- or 93-nm-diameter AgNWs for 24 h with the fluorescence channels set to the indicated probe molecules and using the microscope objectives indicated. Colored numbers show the integrated probe fluorescence intensity. (*D*) Summary of intracellular fluorescent probe quantitation. Error bars report 1 SD on triplicate measurements.

alveolar cells. We covalently attached a pH-sensitive fluorescent dye to commercial silica-coated AgNWs and used time-lapse fluorescence microscopy to observe internalization and intracellular fate. In growth medium, these AgNWs are nonfluorescent, but within about 30 min of exposure they developed a strong green fluorescence indicating uptake into acidifying vesicles (*SI Appendix*, Fig. S2 and Movie S2). We observed multiple examples of punctured phagolysosomes and acid release into the cytoplasm following AgNW internalization (*SI Appendix*, Fig. S8 and Movie S3). We further sought to quantify the extent of endolysosome puncturing in nonimmune cells using the same PVP-coated AgNWs developed for this study. We labeled 60-nm-diameter AgNWs with a histidine-terminated fluorescent protein, mCherry, and coadministered them with established fluorescent probes for endosomes and lysosomes. Following AgNW internalization, the AgNW-mCherry fluorescence only partly colocalizes with endolysosome markers (*SI Appendix*, Fig. S9), providing further evidence of puncturing.

Prior experimental and theoretical studies have investigation the deformation of rod-like vesicle contents including microtubules and multiwalled carbon nanotubes (MWCNTs) that could be caused by lipid bilayer membrane forces (34, 35). Most recently, Zhu et al. (36) used molecular and continuum simulation methods to estimate that MWCNTs could be subjected to forces of up to ∼20 pN during endocytosis and predicted that MWCNTs with a buckling threshold below this value would have a low risk for membrane penetration and permeation. In support of this prediction, studies of the internalization of stiff and flexible MWCNTs reported different intracellular fates and toxicity (36, 37) but these studies could not provide quantitative tests of mechanical forces because the flexible MWCNTs were significantly longer and formed tangled balls. Ji et al. (38) determined a length threshold around 200 nm for proinflammatory response of sub-10-nm-diameter CeO_2 nanorods but did not consider the mechanical interactions or investigate a diameter effect. The present study of AgNWs with the same mean lengths but different mean diameters will allow more quantitative assessment of the hypothesis that membrane forces exerted on internalized fibers can cause deformation (*SI Appendix*). For 10-μm-long AgNWs, the predicted compression forces due to membrane bending elasticity could reach 100 pN, while the linear-rod buckling force requires ∼200 pN. However, the presence of initial curvature, lattice defects and strain or the action of intracellular degradation processes could weaken the AgNWs.

A conceptual model for stiffness dependent AgNW toxicity is given in Fig. 4, and an accompanying quantitative model for the dose-dependence of the cellular cytotoxicity of AgNWs is described in *SI Appendix* and plotted in Fig. 1. Following calibration of the model at low AgNW dose, good agreement with the cell viability data at higher doses supports the concept that cell mortality is determined by the fraction of AgNWs that puncture endolysosome membranes and subsequently undergo surface chemical reactions in the cytosol.

Having established that both diameter and length thresholds affect toxicity, we evaluated key goals for CTN displays: a sheet resistance less than 50 Ω sq^{-1} with an optical transparency greater than 90%. Fig. 1*B* shows the relationship between total transparency and sheet resistance for ∼9-μm-long AgNWs with 3 diameters. Typical AgNWs used for prototype and commercial CTNs have lengths greatly exceeding the threshold for frustrated internalization (5), but the data shown here illustrate that high-conductivity networks can be fabricated with shorter and less hazardous AgNWs. Moreover, at the targeted resistivity, the 3-fold decrease in diameter increases transmission from 92 to 96%. Thus, reducing AgNW diameter is an effective nanomaterial design strategy for lowering cellular injury that can be achieved without a deterioration in target technology performance. Other strategies to lower the hazard from other nanomaterials have been proposed that have not been experimentally proven and that do not consider links to technical performance (39, 40).

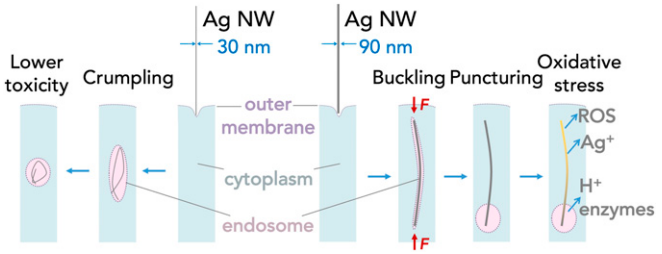

Fig. 4. Conceptual model for a biomechanical threshold causing differential toxicity of AgNW. Both thinner and thicker AgNWs are internalized by endocytosis. (*Left*) Membrane forces during or following endocytosis exceed the yield threshold for thinner AgNW, causing crumpling, containment within the endolysosome and lower toxicity. (*Right*) Membrane forces cannot crumple the thicker AgNW, leading to membrane puncturing and release of endolysosome contents to the cytoplasm and cell toxicity. An associated quantitative model is described in *SI Appendix*.

Our group also seeks to reclaim silver from CNTs using electrochemical methods, and we find no adverse consequences of diameter reduction (*SI Appendix*, Fig. S14). In summary, our findings establish and quantify a biomechanical component to the FPP and suggest that rigidity could be harnessed for nanomedicine approaches to deliver drugs to the cytoplasm (16).

Materials and Methods

Silver Nanowires Synthesis. AgNWs with 3 distinct dimensions were prepared and purified by variations of an established protocol (25). Different quantities of NaCl and poly vinylpyrrolidone (molecular weight = 40,000 g mol^{-1}) were dissolved in ethylene glycol, and slowly added into a stirred solution of $AgNO_3$ in ethylene glycol at room temperature (*SI Appendix*). The mixture was heated to 150 or 160 °C for 60 min and cooled down to room temperature. Reaction temperature and KCl addition was used to control dimensions. Purification by 2 sequential decantations removed by-products and organics. The diameter and length distributions for each batch was determined by SEM imaging. CNTs were fabricated by spray coating AgNW suspensions (Sonotek ExactACoaT). Optical transmittance was measured by UV-visible spectroscopy (Varian Cary 5000) and sheet resistance by a 4-pin probe (Loresta EP MCP-T360).

Cell Culturing and Toxicity Assays. Mouse fibroblast cells (L929) were cultivated in DMEM supplemented with 10% fetal bovine serum, 50 units/mL penicillin, and 50 μg/mL streptomycin (Gibco). Cytotoxicity in L929 cells was assessed using the 3-[4,5-dimethylthiazol-2-yl]-2,5-diphenyl tetrazolium bromide (MTT) assay (Sigma-Aldrich). Briefly, 8,000 cells/well were seeded into a 96-well plate (Nunc) and incubated 37 °C. After 24 h, cells were treated with 100 μL of suspensions containing concentrations between 0.16 to 120 μg/mL of AgNWs or $AgNO_3$ (a positive control for silver toxicity). After a further 24 h, the cells were washed 2 times with phosphate-buffered saline (PBS) and the wells replenished with fresh culture medium containing 0.5 mg/mL of MTT predissolved in PBS. After 3 h of incubation, cells were washed two times with PBS and 100 μL of dimethyl sulfoxide was added to dissolve the formazan crystals. Aliquots were transferred into new well plates to quantify formazan production from the absorbance at 560 nm using a microplate reader (FLUOstar OMEGA, BMG Labtech). Initial trials using cell-free controls and a centrifugation step found that the AgNWs were not transferred in the quantitation step and did not interfere with the assay. The dose–response data for $AgNO_3$ gave excellent agreement with prior studies (26). Cell viability was expressed as percentage relatively to negative control (nontreated cells) using alternative dose metrics: silver mass concentration in *SI Appendix*, Fig. S2 and number of particles per volume in Fig. 1 *C* and *D* and *SI Appendix*, Fig. S4. Viability assays for other cell lines are described in *SI Appendix* and included similar controls.

The impact of AgNW exposure to L929 cells on oxidative stress production, mitochondrial membrane potential, intracellular calcium level and membrane integrity was assessed using fluorescent probes as described in *SI Appendix*. A combination of dark-field and epifluorescent microscopy was used to count the number of internalized AgNWs in L929 cultures exposed to either 30- or 90-nm mean diameter nanowires and to classify the proportion of rod-like or crumpled nanowires (*SI Appendix*, Fig. S3). These data were used to calibrate a statistical model for the dose-dependent viability of murine cells exposed to either 30- or 90-nm mean diameter AgNWs described in *SI Appendix*.

X-Ray Imaging and Chemical Analysis. L929 cells were grown on silicon nitride membrane (Silson) previously coated with poly L-lysine 0.01% (Sigma) in 24-well plate for 24 h before treatment with 33- or 93-nm-diameter, ~10-μm-long, AgNW at a concentration of 10^6 NW/mL for 24 h. After 24 h of treatment, some cell samples were washed with PBS and allow to grow for further 48 h. At the end of the incubation, samples were rinsed with ammonium formate, cryofixed with a Leica EM GP Automatic Plunge Freezer (ESRF) and stored in liquid nitrogen until the analysis.

The distribution of silver and physiological elements was studied by nano-XRF at ID16a at the ESRF (41) under cryogenic conditions. The beam was focused to 26 × 42 nm^2 (vertical × horizontal) using a pair of Kirkpatrick-Baez mirrors. The fluorescence signal emitted from each sample pixel was recorded by a multielement silicon drift detector (SGX Sensortech Ltd.) and fitted with the PyMCA software to generate elemental maps (42). On the same beamline, 2D phase contrast holographic images (43) and 3D tomographic data sets were acquired on selected murine fibroblast cells exposed to 33- or 90-nm-diameter AgNWs. The samples were placed at four distances downstream of the beam focus and the projections recorded at a FReLoN charge-coupled device detector are used to generate phase maps through a phase retrieval algorithm. To obtain 3D data, phase maps at 2,000 rotational angles were used for tomographic reconstruction through filtered back-projection (PyHST). To correct for the wavefront inhomogeneities, random lateral displacements in a given range were applied during the rotation (44). The resulting volume represents the 3D electron density distribution inside the sample, with a voxel size of 15 × 15 × 15 nm.

The chemical speciation of silver in cells exposed to AgNW was studied at ID-21 at the ESRF under cryogenic conditions. The beam was focused to 0.6 × 0.8 μm^2 (vertical × horizontal) using a pair of Kirkpatrick–Baez mirrors. Detectors included a Si_3N_7 diode for I_0 and a silicon drift detector (X-flash Bruker) for the emitted X-ray fluorescence. From rectangular regions of interest, Ag L_{III} edge spectra were generated for each pixel by stacking 2D images acquired at energy steps across the absorption edge. The XANES were aligned using the simpleElastix image registration library (45) and extracted using PyMCA. Bulk XANES spectra of reference compounds and pristine and aged AgNWs were recorded in the unfocused mode under the same conditions and fitted to the experimental data using a least-squares algorithm.

ACKNOWLEDGMENTS. This work was a collaboration between the Charlet group of the Safe(r) Ecodesign Research and Education Applied to Nanomaterial Development (SERENADE) LabEx (S.G.L., D.T., A.-E.P.d.R., M.V., M. Safi, J.-P.S., C.C., L.C., B.G.) and the Nanowire Intelligent Re-Design and Recycling for Environmental Safety (NANOWIR2ES) project (S.G.L., B.O.-S., D.A., C.V., B.G., L.C., A.H.). The SERENADE LabEx project received funding from Excellence Initiative of Aix-Marseille University, a French "Investissements d'Avenir" program. The NANOWIR2ES project received funding from the European Union European Research Area Network Safe Implementation of Innovative Nanoscience and Nanotechnology program and the US Consumer Product Safety Commission. The University of Grenoble–Alpes cofunded (with SERENADE) the Institut des Sciences de la Terre biology lab and an Invited Professor position for B.G. Chemical studies in the B.G. laboratory at Lawrence Berkeley National Laboratory (LBNL) was supported by US Department of Energy Chemical Sciences, Geosciences, and Biosciences Division under Contract DE-AC02-05CH11231. Synchrotron experiments were performed on beamlines ID16A and ID21 at the ESRF, Grenoble, France, under User Proposal LS-2549. We thank Dr. Alejandro Quieruga (LBNL) for discussions on wire mechanics and Dr. Ludovic Lesven (Université de Lille) for advice with electrochemical characterization of AgNWs. We are grateful for the careful review of this manuscript by two anonymous referees.

1. K. Donaldson, F. A. Murphy, R. Duffin, C. A. Poland, Asbestos, carbon nanotubes and the pleural mesothelium: A review of the hypothesis regarding the role of long fibre retention in the parietal pleura, inflammation and mesothelioma. *Part. Fibre Toxicol.* **7**, 5 (2010).
2. K. Donaldson, C. L. Tran, An introduction to the short-term toxicology of respirable industrial fibres. *Mutat. Res.* **553**, 5–9 (2004).
3. A. B. Kane, R. H. Hurt, Nanotoxicology: The asbestos analogy revisited. *Nat. Nanotechnol.* **3**, 378–379 (2008).
4. D. Langley *et al.*, Flexible transparent conductive materials based on silver nanowire networks: A review. *Nanotechnology* **24**, 452001 (2013).
5. T. Sannicolo *et al.*, Metallic nanowire-based transparent electrodes for next generation flexible devices: A review. *Small* **12**, 6052–6075 (2016).
6. M. Cann *et al.*, High performance transparent multi-touch sensors based on silver nanowire. *Mater. Today Commun.* **7**, 42–50 (2016).
7. L. D. Scanlan *et al.*, Silver nanowire exposure results in internalization and toxicity to *Daphnia magna*. *ACS Nano* **7**, 10681–10694 (2013).
8. R. M. Silva *et al.*, Short versus long silver nanowires: A comparison of in vivo pulmonary effects post instillation. *Part. Fibre Toxicol.* **11**, 52 (2014).
9. S. G. Lehmann *et al.*, In vitro dermal safety assessment of silver nanowires after acute exposure: Tissue vs. cell models. *Nanomaterials (Basel)* **8**, 232 (2018).
10. L. C. Stoehr *et al.*, Shape matters: Effects of silver nanospheres and wires on human alveolar epithelial cells. *Part. Fibre Toxicol.* **8**, 36 (2011).
11. A. Schinwald, K. Donaldson, Use of back-scatter electron signals to visualise cell/nanowires interactions in vitro and in vivo; frustrated phagocytosis of long fibres in macrophages and compartmentalisation in mesothelial cells in vivo. *Part. Fibre Toxicol.* **9**, 34 (2012).
12. N. K. Verma *et al.*, Autophagy induction by silver nanowires: A new aspect in the biocompatibility assessment of nanocomposite thin films. *Toxicol. Appl. Pharmacol.* **264**, 451–461 (2012).
13. I. G. Theodorou *et al.*, Silver nanowire particle reactivity with human monocyte-derived macrophage cells: Intracellular availability of silver governs their cytotoxicity. *ACS Biomater. Sci. Eng.* **3**, 2336–2347 (2017).
14. A. Schinwald, T. Chernova, K. Donaldson, Use of silver nanowires to determine thresholds for fibre length-dependent pulmonary inflammation and inhibition of macrophage migration in vitro. *Part. Fibre Toxicol.* **9**, 47 (2012).
15. S. Chen *et al.*, Sulfidation of silver nanowires inside human alveolar epithelial cells: A potential detoxification mechanism. *Nanoscale* **5**, 9839–9847 (2013).

16. M. Singh, D. Movia, O. K. Mahfoud, Y. Volkov, A. Prina-Mello, Silver nanowires as prospective carriers for drug delivery in cancer treatment: An in vitro biocompatibility study on lung adenocarcinoma cells and fibroblasts. *Eur. J. Nanomed.* **5**, 195–204 (2013).
17. R. F. Hamilton, Jr *et al*., Particle length-dependent titanium dioxide nanomaterials toxicity and bioactivity. *Part. Fibre Toxicol.* **6**, 35 (2009).
18. L. Y. T. Chou, K. Ming, W. C. W. Chan, Strategies for the intracellular delivery of nanoparticles. *Chem. Soc. Rev.* **40**, 233–245 (2011).
19. X. Shi, A. von dem Bussche, R. H. Hurt, A. B. Kane, H. Gao, Cell entry of one-dimensional nanomaterials occurs by tip recognition and rotation. *Nat. Nanotechnol.* **6**, 714–719 (2011).
20. H. Ewers *et al*., GM1 structure determines SV40-induced membrane invagination and infection. *Nat. Cell Biol.* **12**, 11–18 (2010).
21. R. Y. Chen *et al*., Co-percolating graphene-wrapped silver nanowire network for high performance, highly stable, transparent conducting electrodes. *Adv. Funct. Mater.* **23**, 5150–5158 (2013).
22. S. Sorel, P. E. Lyons, S. De, J. C. Dickerson, J. N. Coleman, The dependence of the optoelectrical properties of silver nanowire networks on nanowire length and diameter. *Nanotechnology* **23**, 185201 (2012).
23. S. M. Bergin *et al*., The effect of nanowire length and diameter on the properties of transparent, conducting nanowire films. *Nanoscale* **4**, 1996–2004 (2012).
24. Y. G. Sun, B. Gates, B. Mayers, Y. N. Xia, Crystalline silver nanowires by soft solution processing. *Nano Lett.* **2**, 165–168 (2002).
25. C. Mayousse *et al*., Improvements in purification of silver nanowires by decantation and fabrication of flexible transparent electrodes. Application to capacitive touch sensors. *Nanotechnology* **24**, 215501 (2013).
26. J. Jiravova *et al*., The effect of silver nanoparticles and silver ions on mammalian and plant cells in vitro. *Food Chem. Toxicol.* **96**, 50–61 (2016).
27. A. Manke, L. Wang, Y. Rojanasakul, Mechanisms of nanoparticle-induced oxidative stress and toxicity. *BioMed Res. Int.* **2013**, 942916 (2013).
28. A. Nel, T. Xia, L. Mädler, N. Li, Toxic potential of materials at the nanolevel. *Science* **311**, 622–627 (2006).
29. C. Levard, E. M. Hotze, G. V. Lowry, G. E. Brown, Jr, Environmental transformations of silver nanoparticles: Impact on stability and toxicity. *Environ. Sci. Technol.* **46**, 6900–6914 (2012).
30. U. Shefa, M. S. Kim, N. Y. Jeong, J. Jung, Antioxidant and cell-signaling functions of hydrogen sulfide in the central nervous system. *Oxid. Med. Cell. Longev.* **2018**, 1873961 (2018).
31. M. Bunderson-Schelvan, A. Holian, R. F. Hamilton, Jr, Engineered nanomaterial-induced lysosomal membrane permeabilization and anti-cathepsin agents. *J. Toxicol. Environ. Health B Crit. Rev.* **20**, 230–248 (2017).
32. H. J. Jung *et al*., Silver wire amplifies the signaling mechanism for IL-1beta production more than silver submicroparticles in human monocytic THP-1 cells. *PLoS One* **9**, e112256 (2014).
33. B. Sun *et al*., NADPH oxidase-dependent NLRP3 inflammasome activation and its important role in lung fibrosis by multiwalled carbon nanotubes. *Small* **11**, 2087–2097 (2015).
34. D. K. Fygenson, J. F. Marko, A. Libchaber, Mechanics of microtubule-based membrane extension. *Phys. Rev. Lett.* **79**, 4497–4500 (1997).
35. A. E. Cohen, L. Mahadevan, Kinks, rings, and rackets in filamentous structures. *Proc. Natl. Acad. Sci. U.S.A.* **100**, 12141–12146 (2003).
36. W. Zhu *et al*., Nanomechanical mechanism for lipid bilayer damage induced by carbon nanotubes confined in intracellular vesicles. *Proc. Natl. Acad. Sci. U.S.A.* **113**, 12374–12379 (2016).
37. H. Nagai *et al*., Diameter and rigidity of multiwalled carbon nanotubes are critical factors in mesothelial injury and carcinogenesis. *Proc. Natl. Acad. Sci. U.S.A.* **108**, E1330–E1338 (2011).
38. Z. Ji *et al*., Designed synthesis of CeO_2 nanorods and nanowires for studying toxicological effects of high aspect ratio nanomaterials. *ACS Nano* **6**, 5366–5380 (2012).
39. E. K. Jensen, S. Y. Larsen, U. C. Nygaard, C. D. Marioara, T. Syversen, Early combination of material characteristics and toxicology is useful in the design of low toxicity carbon nanofiber. *Materials (Basel)* **5**, 1560–1580 (2012).
40. R. Li *et al*., Surface interactions with compartmentalized cellular phosphates explain rare earth oxide nanoparticle hazard and provide opportunities for safer design. *ACS Nano* **8**, 1771–1783 (2014).
41. J. C. Da Silva, *et al*., Efficient concentration of high-energy x-rays for diffraction-limited imaging resolution. *Optica* **4**, 492–495 (2017).
42. V. A. Sole, E. Papillon, M. Cotte, P. Walter, J. Susini, A multiplatform code for the analysis of energy-dispersive X-ray fluorescence spectra. *Spectrochim. Acta B Atom. Spectrosc.* **62**, 63–68 (2007).
43. P. Cloetens *et al*., Holotomography: Quantitative phase tomography with micrometer resolution using hard synchrotron radiation x rays. *Appl. Phys. Lett.* **75**, 2912–2914 (1999).
44. M. Hubert *et al*., Efficient correction of wavefront inhomogeneities in X-ray holographic nanotomography by random sample displacement. *Appl. Phys. Lett.* **112**, 203704 (2018).
45. K. Marstal, F. Berendsen, M. Staring, S. Klein, SimpleElastix: A user friendly, multilingual library for medical image registration. *IEEE Conference on Computer Vision and Pattern Recognition Workshops*, 10.1109/CVPRW.2016.78 (2016).